SCIENTIFIC REPORTS
natureresearch

OPEN

Atomic layer deposition of ZnO/TiO₂ nanolaminates as ultra-long life anode material for lithium-ion batteries

Yan-Qiang Cao, Shan-Shan Wang, Chang Liu, Di Wu & Ai-Dong Li

In this work, we designed ZnO/TiO₂ nanolaminates by atomic layer deposition (ALD) as anode material for lithium ion batteries. ZnO/TiO₂ nanolaminates were fabricated on copper foil by depositing unit of 26 cycles ZnO/26 cycles TiO₂ repeatedly using ALD. ZnO/TiO₂ nanolaminates are much more stable than pristine ZnO films during electrochemical cycling process. Therefore, ZnO/TiO₂ nanolaminates exhibit excellent lithium storage performance with an improved cycling performance and superior rate capability compared to pristine ZnO films. Moreover, coulombic efficiency (CE) of ZnO/TiO₂ nanolaminates is above 99%, which is much higher than the value of pristine ZnO films. Excellent ultralong-life performance is gained for ZnO/TiO₂ nanolaminates, retaining a reversible capacity of ~667 mAh g^{-1} within cut-off voltage of 0.05-2.5 V after 1200 cycles of charge-discharge at 500 mA g^{-1}. Constructing nanolaminates structures via ALD might open up new opportunities for improving the performance of anode materials with large volume expansion in lithium ion batteries.

Rechargeable lithium ion batteries (LIBs) have attracted great attentions in energy storage area due to their high energy density and benign cycling life[1–4]. However, the current commercially used graphite anode with a relatively low theoretical capacity of 372 mAh g^{-1} cannot satisfy the increasing needs of the ever-enlarging market, especially in hybrid electric vehicles and electric vehicles. Therefore, transition metal oxides with higher theoretical capacities are intensively investigated as alternative anode to graphite[5–10]. Among them, zinc oxide (ZnO) exhibits promising properties, such as environmental benignity, high theoretical capacity (987 mAh g^{-1}), as well as higher lithium ion diffusion coefficient compared to other transition metal oxides[11–13]. Nevertheless, ZnO electrodes usually suffer from poor electronic conductivity and huge volume change (228%) during lithiation and delithiation, resulting in poor electrochemical reaction kinetics and severe pulverization along with inferior cyclic stability and rate capability[14,15]. Therefore, rational design of high performance ZnO based anode for LIBs still remains a challenge. To this regard, great efforts have been devoted to improving the performance of ZnO anode, such as construction of various nanostructured electrodes and modification of ZnO[16–21]. For example, Xie *et al.* reported a ZnO based nanostructured anode of sandwich-like Ag-C@ZnO-C@Ag-C hybrid hollow microspheres, which exhibits a large reversible capacity of 1670 mAh g^{-1} after 200 cycles at a current density of 200 mA g^{-1} with excellent high-rate performance. The special structural features, including hollow structures, the sandwich-like shells, and the nanoscale dimension, contribute to the outstanding electrochemical performance[22].

Atomic layer deposition (ALD) is a novel and promising thin film deposition technique based on sequential self-limited and complementary surface chemisorption reactions, which is able to deposit ultrathin, uniform, and conformal layers with precise thickness control[23,24]. This novel method has shown great prospects in preparation and modification of materials in energy area[25,26], including anodes[27,28], cathodes[29,30], solid electrolytes[31–33] of Li-ion batteries, as well as supercapacitors[34]. ALD has been used to improve the performance of ZnO anodes via depositing active ZnO onto carbon based supporters (graphene, carbon black, carbon foam, etc.)[12,35] and surface modification[36]. For example, Zhao *et al.* reported that 3D carbon/ZnO nanomembrane foam prepared by ALD can retain 92% capacity after 700 cycles at 2 A g^{-1} and deliver a remarkable areal capacity of 4.3 mAh cm^{-2}[35]. Lu *et*

National Laboratory of Solid State Microstructures, Jiangsu Key Laboratory of Artificial Functional Materials, Materials Science and Engineering Department, College of Engineering and Applied Sciences, Collaborative Innovation Center of Advanced Microstructures, Nanjing University, Nanjing, 210093, P. R. China. Correspondence and requests for materials should be addressed to A.-D.L. (email: adli@nju.edu.cn)
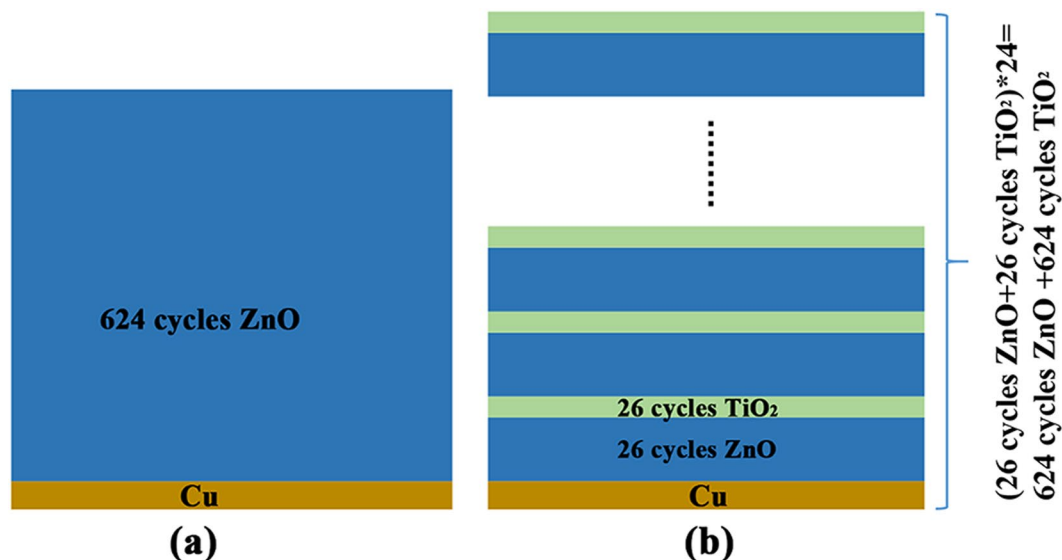
Figure 1. Schematic structure of (**a**) pristine ZnO films and (**b**) ZnO/TiO$_2$ nanolaminates prepared by ALD.

al. fabricated ZnO-carbon black nanocomposites by directly depositing ZnO on carbon black using ALD, which exhibit excellent cyclic stability with a specific capacity of 1026 mAh g^{-1} maintained after 500 cycles[12]. Shi *et al.* utilized ALD Al$_2$O$_3$ coating to stabilize ZnO-graphene anode, which can maintained a reversible specific capacity of ~490 mAh g^{-1} after 100 cycles[36].

Besides, ALD is a very powerful technique to construct novel nanostructures, various nanostructured electrodes have been designed and fabricated by ALD[37]. Nanolaminates are composite films consisted of alternating layers of different materials with individual layer thicknesses down to nanometer scale. ALD is ideally suited for fabricating nanolaminate films due to its precise thickness control of ~1 Å for the individual layers in the composites[38]. Herein, we designed the novel ZnO/TiO$_2$ nanolaminates as anode materials for LIBs. ZnO/TiO$_2$ nanolaminates were fabricated directly on copper foil by depositing 24 units of 26 cycles ZnO/26 cycles TiO$_2$ repeatedly using ALD. Herein, ZnO is the main active material, providing high capacity. While, the inserted TiO$_2$ layers are designed to stabilize ZnO from the following two considerations. Firstly, TiO$_2$ can divide thick ZnO into multi-nanolayers, the dimension (thickness) of each ZnO layer is reduced to nanometer scale. Secondly, TiO$_2$ is stable during charging-discharging process with the volume change of only 4%[39,40]. Therefore, the stable TiO$_2$ thin films can also act as protective layers for ZnO. Accordingly, the electrochemical tests demonstrate that the reversible capacity and the rate performance of ZnO films are greatly improved after inserting TiO$_2$ thin films. Moreover, ZnO/TiO$_2$ nanolaminates exhibit excellent ultralong-life performance, retaining a reversible capacity of ~667 mAh g^{-1} almost without decay after 1200 cycles of charge-discharge at 500 mA g^{-1} with upper cut-off voltage of 2.5 V. Therefore, ZnO/TiO$_2$ nanolaminates can work as ultra-long lifespan anodes in LIBs.

Results

ZnO/TiO$_2$ nanolaminates with ZnO/TiO$_2$ thickness ratio of ~5:1 was designed. Considering the growth rate per cycle (GPC) is around 1.75 Å for ZnO and 0.36 Å for TiO$_2$ in our system[41,42], the nanolaminate was fabricated by depositing 24 alternate layers of ZnO (26 cycles) and TiO$_2$ (26 cycles) with ZnO as the beginning layer. The schematic of ALD deposition process for ZnO/TiO$_2$ nanolaminates is shown in Fig. S1. For comparison, the control sample of pristine ZnO film (624 cycles ZnO) was also prepared. Both samples were deposited directly onto Cu foil. The structure of samples are showed in Fig. 1.

SEM was performed to observe the surface morphology of pristine ZnO films and ZnO/TiO$_2$ nanolaminates. In Fig. 2(a), it can be seen that pristine ZnO films deposited by ALD exhibit a lot of spindly grains with ~15 nm × 55 nm. After inserting TiO$_2$ interlayer, ZnO/TiO$_2$ nanolaminates show distinct morphology with much larger grain size of ~170 nm, as shown in Fig. 2(b). The grain size distribution is presented in Fig. S2 and S3. Due to the excellent conformality and uniformity of ALD, both films can cover the Cu foil conformally. EDS measurement in Fig. S4 provides the evidence for the presence of Zn, Ti, and O elements. In addition, the element mappings by EDS for the ZnO/TiO$_2$ nanolaminates are also conducted, as shown in Fig. 2(c–e), which indicate that Zn, Ti and O elements are uniformly distributed over the whole surface. Moreover, the thickness is determined to be around 104 nm and 132 nm for pristine ZnO films and ZnO/TiO$_2$ nanolaminates, respectively, from the cross-section FESEM images (Fig. S5). The crystallinity of as deposited ZnO and ZnO/TiO$_2$ nanolaminates were also characterized by XRD, as shown in Fig. S6. It can be seen that as-deposited ZnO shows a weak (002) peak from hexagonal wurtzite ZnO. However, no peaks assigned to ZnO or TiO$_2$ can be observed for ZnO/TiO$_2$ nanolaminates. Inserting amorphous Al$_2$O$_3$ layer can inhibit the ZnO crystal growth has been reported by Elam *et al.*[38]. Therefore, amorphous TiO$_2$ here can also reduce the crystallinity of ZnO.

The composition and chemical state of the ZnO/TiO$_2$ nanolaminates were evaluated via XPS. The Zn 2p, Ti 2p and O 1s signals centred at 1021.5, 458.7, and 529.9 eV can be easily found in the survey spectrum, revealing the coexistence of Zn, Ti and O in ZnO/TiO$_2$ nanolaminates (Fig. 3a). In Fig. 3(b), Zn 2p exhibits two distinct
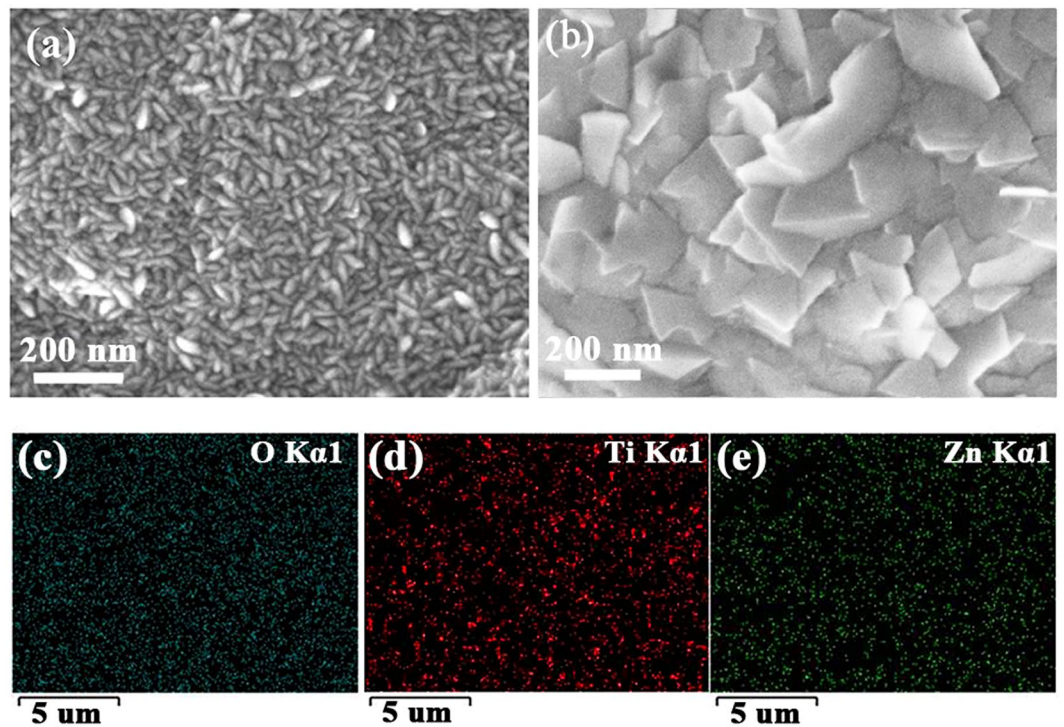
Figure 2. SEM images of (**a**) pristine ZnO films and (**b**) ZnO/TiO$_2$ nanolaminates, (**c**–**e**) SEM element mapping results of ZnO/TiO$_2$ nanolaminates.
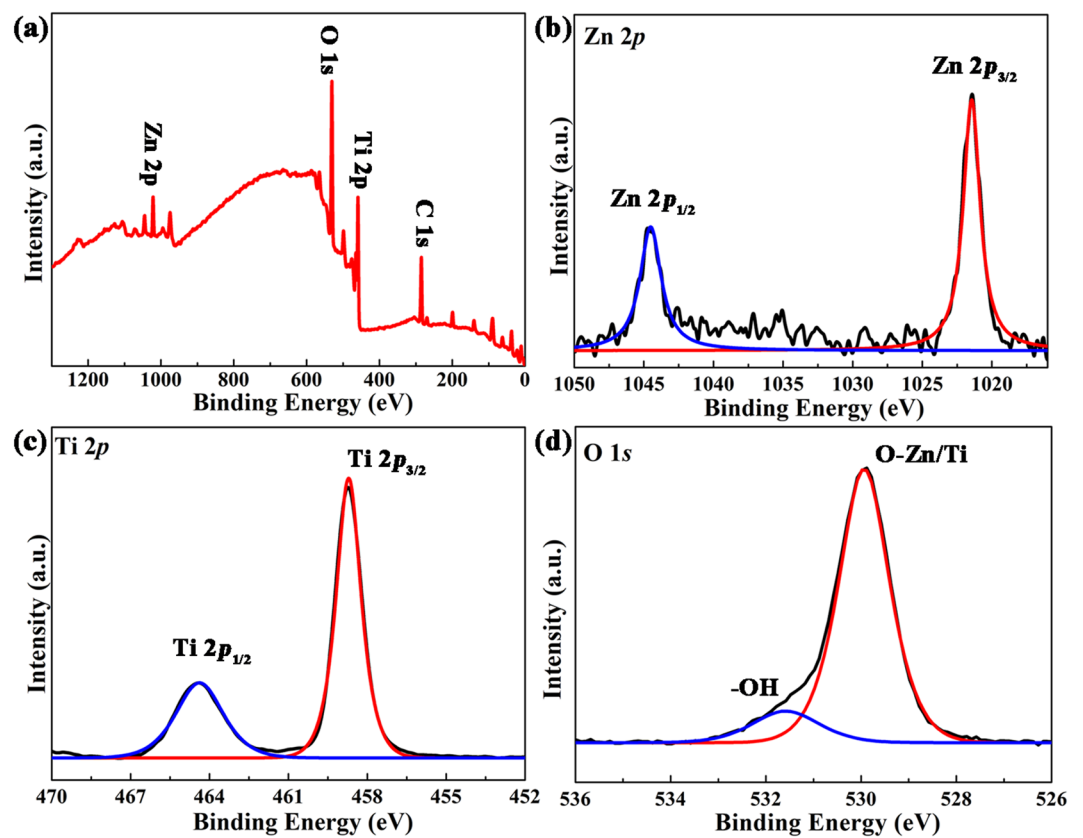

Figure 3. (**a**) The XPS survey spectra, high resolution (**b**) Zn 2p, (**c**) Ti 2p, and (**d**) O 1 s XPS spectra of ZnO/TiO$_2$ nanolaminates.
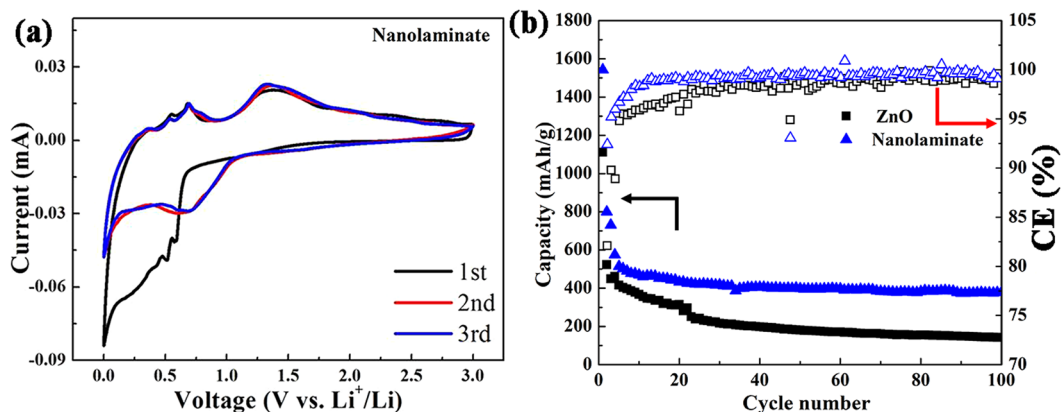
Figure 4. CV curves of (**a**) ZnO/TiO$_2$ nanolaminates electrodes for the initial three cycles at the scan rate of 0.3 mV/s in the voltage range of 0–3 V. (**b**) Cycling performance and CE of ZnO/TiO$_2$ nanolaminates and pristine ZnO films at 500 mA g^{-1} for 100 cycles in the potential range of 0.05–2.0 V.

peaks at 1044.5 eV and 1021.5 eV, which can be assigned to Zn 2p$_{1/2}$ and Zn 2p$_{3/2}$ peaks of Zn-O bonding with the spin orbit splitting energy of 23.0 eV, in good agreement with the value for ZnO[43]. In Fig. 3(c), the doublet with at 464.4 eV and 458.7 eV corresponds to Ti 2p$_{1/2}$ and Ti 2p$_{3/2}$ of Ti-O bonding with the spin orbit splitting energy of 5.7 eV, consistent with the value of TiO$_2$[44]. The spectrum of O 1 s (Fig. 3d) shows the main peak for O-Zn/O-Ti bonds of ZnO/TiO$_2$ at 529.9 eV, the position of O-Zn and O-Ti are too close to be distinguished[45,46]. Besides, the peak related to -OH on the surface of ZnO/TiO$_2$ nanolaminates at 531.6 eV can also be detected[47]. Both SEM EDS and XPS spectra can confirm that ZnO and TiO$_2$ coexist in the films. In addition, the Zn/Ti atom distribution was also measured by XPS depth profile, as shown in Fig. S7, the multilayer structure of ZnO/TiO$_2$ nanolaminates can be recognized. Cross-sectional TEM images also confirm the layer-by-layer structure of ZnO/TiO$_2$ nanolaminates, as shown in Fig. S8.

Figure 4(a) shows the cyclic voltammograms (CV) of ZnO/TiO$_2$ nanolaminates anode for the initial three cycles. Based on the previous literatures, the electrochemical process of ZnO towards lithium can be described as the following reactions[48]:

$$ZnO + 2Li^+ + 2e^- \leftrightarrow Li_2O + Zn \tag{1}$$

$$Zn + xLi^+ + xe^- \leftrightarrow Li_xZn \ (x \leq 1) \tag{2}$$
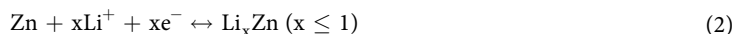
For ZnO/TiO$_2$ nanolaminates, there are two small shoulders at ~0.59 V and 0.51 V as well as a broad peak centred at ~0.30 V can be discerned during the first cathodic scan. The shoulder at 0.59 V is derived from the decomposition of liquid electrolyte to form a solid electrolyte interphase (SEI) layer[49,50]. According to previous reports, the conversion reaction between ZnO and Li ion to generate Zn and Li$_2$O generally takes place at ~0.50 V, while the subsequent alloying reaction between Zn and Li ion to produce Li$_x$Zn alloys at around 0.25 V[11]. Two above-mentioned electrochemical reactions overlap partially here, therefore, a broad reduction peak centred at ~0.30 V and a small shoulder near 0.51 V can be observed. This phenomenon can be commonly observed in many other ZnO-based anodes[22,36,51]. In the subsequent first anodic scan, three peaks located between 0.20–0.80 V (0.36 V, 0.53 V and 0.79 V) are ascribed to the multistep dealloying process of Li$_x$Zn alloy[13]. Another broad peak at 1.32 V can be related to the formation of ZnO by the redox reaction between Li$_2$O and Zn[52]. In the subsequent two cycles, the CV curves show very good reproducibility, indicating high reversibility and excellent cycling stability of ZnO/TiO$_2$ nanolaminates. The CV curves of pristine ZnO films shown in Fig. S9 are similar to those of ZnO/TiO$_2$ nanolaminates. However, pristine ZnO films exhibit worse cycling stability than ZnO/TiO$_2$ nanolaminates, as indicated with reduced enclosed CV area. In addition, pristine ZnO films exhibit an irreversible anodic peak at ~2.7 V, corresponding to the oxidation process of Zn back to ZnO. This peak disappears after 2 cycles, indicating the conversion reaction is irreversible for ZnO, same phenomenon has been observed in previous literature[53].

Figure 4(b) plots the cycling performance of ZnO/TiO$_2$ nanolaminates and pristine ZnO films at 500 mA g^{-1} for 100 cycles in the potential range of 0.05–2.0 V. It can be seen that the capacity of ZnO/TiO$_2$ nanolaminates only drops in the initial few cycles, and then maintains a relatively stable capacity. Therefore, ZnO/TiO$_2$ nanolaminates can maintain a reversible capacity of 381 mAh g^{-1} after 100 cycles at 500 mA g^{-1}, demonstrating its excellent cycling performance. In contrast, pristine ZnO films exhibit a decreasing capacity along with cycling, only about 141 mAh g^{-1} can be remained after 100 cycles. Obviously, the cycling performance of ZnO/TiO$_2$ nanolaminates is much better than pristine ZnO films. Fig. S10 exhibits the discharge/charge profiles ZnO and ZnO/TiO$_2$ nanolaminates at 500 mA g^{-1} with cut-off potential of 0.05–2.0 V in 1st, 2rd, 3th, 50th and 100th cycle. More importantly, the CE of ZnO/TiO$_2$ nanolaminates is above 99%, which is much higher than the value of pristine ZnO films. Especially in first 20 cycles, for example, the CE at 15th cycle is 99.0% and 96.2% for ZnO/TiO$_2$ nanolaminates and pristine ZnO films, respectively. The cycling performance was also conducted at the current density of 200 mA g^{-1}, as shown in Fig. S11 and S12, which shows the similar phenomena.
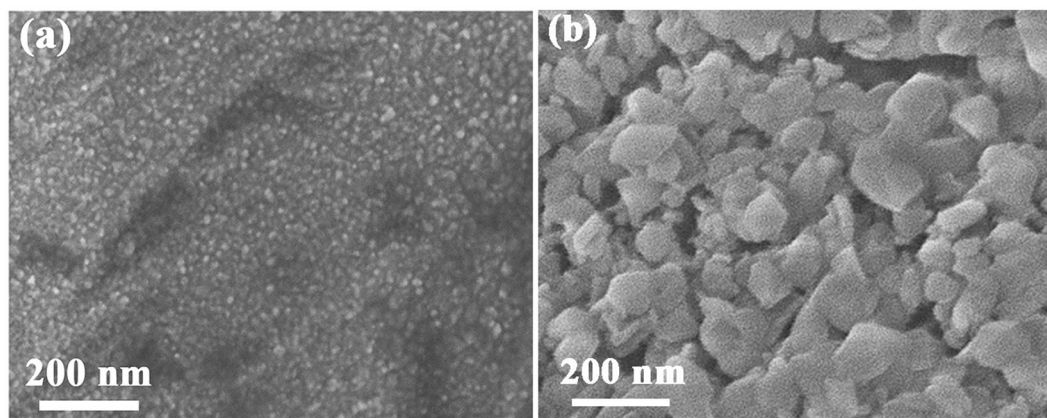
Figure 5. SEM images of (**a**) pristine ZnO films and (**b**) ZnO/TiO$_2$ nanolaminates after 100 cycles charging-discharging at 200 mA g^{-1}.
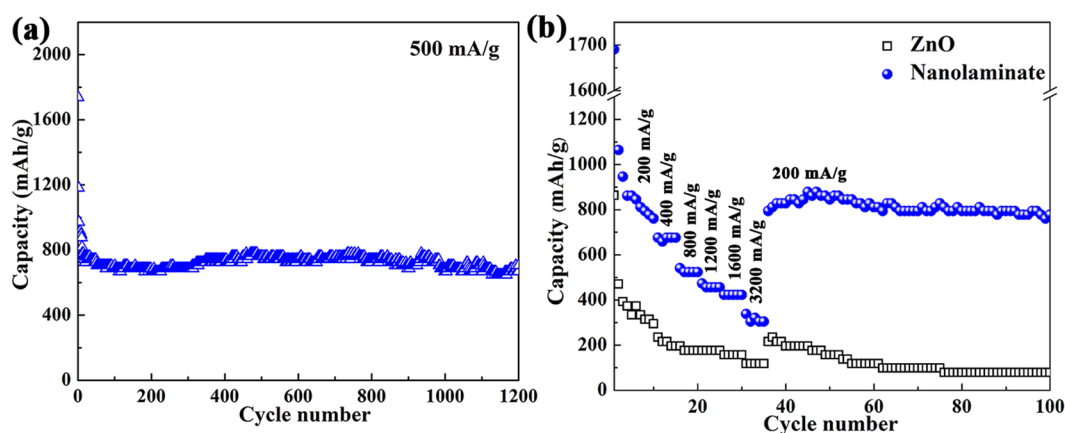

Figure 6. (**a**) Ultra-long cycling performance of ZnO/TiO$_2$ nanolaminates at 500 mA g^{-1} for 1200 cycles in the potential range of 0.05–2.5 V. (**b**) Comparison of rate capability for ZnO/TiO$_2$ nanolaminates and pristine ZnO films anodes in the potential range of 0.05–2.5 V.

In order to explore the mechanism of enhanced electrochemical performance, SEM was performed to observe the morphology change after charging-discharging process. Figure 5(a) shows the SEM image of pristine ZnO films after 100 cycles cycling at the current density of 200 mA g^{-1}. It can be seen that the spindly grains of ZnO are disappeared after cycling, leaving lots of small particles with the size less than 10 nm. It implies that the pulverization is very severe for pristine ZnO film during cycling. It has been demonstrated in previous reports that ZnO materials possess large volume expansion (228%) upon cycling, which would lead to severe pulverization for ZnO[11,13]. In contrast, the morphology of ZnO/TiO$_2$ nanolaminates is much more stable than pristine ZnO, as shown in Fig. 5(b). Although the pulverization of grains still can be observed after cycling, large grain of ZnO/TiO$_2$ nanolaminates is almost retained, suggesting its superior structural stability. Even cycled at high current density of 500 mA g^{-1} for 100 cycles, ZnO/TiO$_2$ nanolaminates can still maintain its structure, as shown in Fig. S13. In addition, EDS was also conducted for ZnO/TiO$_2$ nanolaminates after 100 cycling of 500 mA g^{-1}, as shown in Fig. S14. It can be seen that Zn, Ti, O elements are still uniformly distributed after cycling. It can be demonstrated that ZnO/TiO$_2$ nanolaminates are much more stable than pristine ZnO films.

Furthermore, we also explore the effect of cut-off voltage on the performance of ZnO/TiO$_2$ nanolaminates. Therefore, cycling performance was also conducted in the potential range of 0.05–2.5 V for comparison, as shown in Fig. S15. It can be easily seen that larger cycling potential range delivers higher capacity. Moreover, ZnO/TiO$_2$ nanolaminates can still show great cycling stability, exhibiting a reversible capacity of 875 and 706 mAh g^{-1} after 100 cycles at 200 and 500 mA g^{-1}, respectively. Therefore, long-life cycling and rate capability were also performed in the potential range of 0.05–2.5 V. Figure 6(a) plots the long-life cycling performance conducted at 500 mA g^{-1} for 1200 cycles within the voltage of 0.05–2.5 V. The capacity only decreases at the initial several cycles. After that, the reversible capacity can be stabilized at ~667 mAh g^{-1} almost without decay, revealing a remarkable long-life performance. The rate capability of ZnO/TiO$_2$ nanolaminates was also evaluated, as shown in Fig. 6(b), which was performed from 200 mA g^{-1} to 3200 mA g^{-1}. It can be clearly seen that the ZnO/TiO$_2$ nanolaminates exhibit excellent capacity retention at various current densities. Even at a high current density of 3200 mA g^{-1}, a high capacity of ~307 mAh g^{-1} can be achieved, demonstrating a superior high-rate performance of ZnO/TiO$_2$
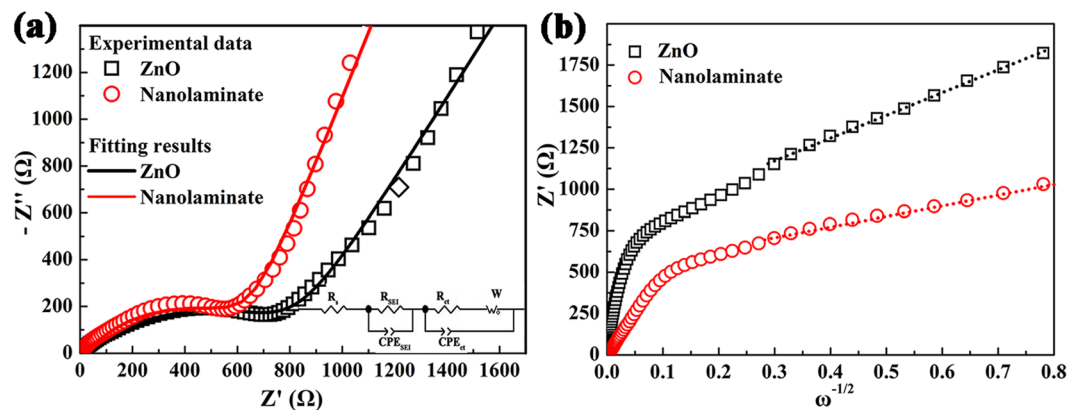
Figure 7. (**a**) Nyquist plots and (**b**) Randles plots of ZnO films and ZnO/TiO$_2$ nanolaminates. The insert of (**a**) is the equivalent circuit model for EIS fitting.

Electrode	R$_s$ (Ω)	R$_{SEI}$ (Ω)	R$_{ct}$ (Ω)	σ$_w$
ZnO	3.5	25.1	804.5	1394.0
Nanolaminate	2.8	19.6	590.2	642.6

Table 1. EIS fitting data of pristine ZnO films and ZnO/TiO$_2$ nanolaminate electrodes.

nanolaminates. Furthermore, the cell is able to deliver a reversible capacity of 750 mAh g^{-1} when the current density returns back to 200 mA g^{-1}. While pristine ZnO films show very poor rate ability.

To explore the charge transfer and Li ion diffusion characteristics in the pristine ZnO films and ZnO/TiO$_2$ nanolaminates, EIS measurements were further conducted. Figure 7(a) compares the Nyquist plots of ZnO films and ZnO/TiO$_2$ nanolaminates. Obviously, both Nyquist plots exhibit a semicircle in the high-middle frequency region and a slop line in the low frequency region. According to the reported literatures, the semicircle in high-frequency region is ascribed to the formation of the SEI layer and contacting impedance between active materials and electrolyte, the semicircle in the middle frequency range is assigned to the charge-transfer resistance (R$_{ct}$) of electrode/electrolyte interface. The slopping line in low frequency region corresponds to diffusion of Li ion in electrodes[54]. Therefore, the EIS data were fitted using the mode of the insert in Fig. 7(a)[55]. Herein, R$_s$, R$_{SEI}$, and R$_{ct}$ represent electrolyte resistance, SEI resistance, and charge-transfer resistance, respectively. CPE is the respective constant-phase element contributing to the semicircle in the experimental spectra. And W is the Warburg impedance. The fitted data are listed in Table 1. The SEI resistance and the charge-transfer resistance of the ZnO/TiO$_2$ nanolaminates are lower than pristine ZnO films. Furthermore, Randles plots (Warburg impedance (Z$_w$) vs. ω$^{-1/2}$) of both electrodes were built, as shown in Fig. 7(b), where the slope of the fitted line in low frequency region is the Warburg coefficient (σ$_w$)[56]. The diffusion coefficient of Li ion (D$_{Li}$+) is inversely proportional to σ$_w^2$[57,58]. Obviously, the value of σ$_w$ for ZnO/TiO$_2$ nanolaminates electrodes is smaller than that of ZnO films electrodes, thereby possessing higher D$_{Li}$+. It is observed that the Warburg coefficients (σ$_w$) of ZnO films and ZnO/TiO$_2$ nanolaminates electrodes are 1394.0 and 642.6, respectively. The EIS measurements indicate that the formation of ZnO/TiO$_2$ nanolaminates can decrease the SEI resistance and charge-transfer resistance, as well as improve the solid state Li ion diffusion in ZnO electrode. Accordingly, the superior lithium storage characteristics are exhibited in ZnO/TiO$_2$ nanolaminates electrode compared to pristine ZnO films.

The excellent electrochemical performance of ZnO/TiO$_2$ nanolaminates as anodes of LIBs can be ascribed to the following factors. (1) The dimension (thickness) of each active ZnO layer is reduced to nanometer scale. (2) Moreover, each active ZnO layers are protected by stable thin TiO$_2$ layers from both side. Both above two factors can contribute to improving the stability of ZnO, therefore a remarkable electrochemical performance can be achieved.

Conclusions

In summary, a novel nanostructured anode of ZnO/TiO$_2$ nanolaminates was developed in this work, which was constructed by depositing unit of 26 cycles ZnO/26 cycles TiO$_2$ repeatedly using ALD. It is demonstrated that ZnO/TiO$_2$ nanolaminates are much stable than pristine ZnO films during electrochemical cycling process. Accordingly, the electrochemical tests demonstrate that the reversible capacity and the rate performance of ZnO films are greatly improved after inserting TiO$_2$ thin films. Moreover, ZnO/TiO$_2$ nanolaminates exhibit excellent ultralong-life performance, retaining a reversible capacity of ~667 mAh g^{-1} in potential range of 0.05–2.5 V almost without decay after 1200 cycles of charge-discharge at 500 mA g^{-1}. In addition, EIS measurements indicate that the formation of ZnO/TiO$_2$ nanolaminates can decrease the SEI resistance and charge-transfer resistance, as well as improve the solid state Li ion diffusion in bulk electrode. Above results imply that constructing nanolaminates structures via ALD might open up new opportunities for improving the performance of anode materials with large volume change in LIBs. ALD exhibits excellent large area uniformity, conformality, and precise

thickness control. Therefore, it is very suitable for large scale fabrication. However, the cost of ALD may be too expensive to be used in LiBs for active materials deposition at present. Nowadays, various new type of ALD are researched to solve the cost problem, such as spatial ALD. We believe that ALD will play an important role in energy area in soon future.

Methods

Fabrication of ZnO/TiO$_2$ nanolaminates.
In ALD process, diethyl zinc (DEZ, 6N, Nata Opto-electronic Material Co., Ltd), titanium tetrachloride (TiCl$_4$, 5N, Suzhou Fornano Corporation Ltd.) and deionized water were used as Zn, Ti precursors and oxygen source, respectively. All the precursors were kept at room temperature. Pure N$_2$ (5N) was used as carrier and purge gas. ALD process was performed at 130 °C in a commercial Picosun SUNALE™ R-200 ALD reactor. ZnO/TiO$_2$ nanolaminates were fabricated through an alternate deposition of ZnO and TiO$_2$ by ALD. Pulse time of three precursors was 0.1 s with a 4 s N$_2$ purging step to remove the redundant reactants and by-products. In our ALD systems, the growth rate per cycle (GPC) is around 1.75 Å for ZnO and 0.36 Å for TiO$_2$[41,42]. Herein, we designed the ZnO/TiO$_2$ nanolaminates with ZnO/TiO$_2$ thickness ratio of around 5:1. Therefore, the nanolaminate was fabricated by depositing 24 alternate layers of ZnO (26 cycles) and TiO$_2$ (26 cycles) with ZnO as the beginning layer. For comparison, the control sample of pristine ZnO film (624 cycles ZnO) was also prepared. Both samples were deposited directly onto Cu foil.

Materials characterizations.
The surface chemical features were investigated by X-ray photoelectron spectroscopy (XPS, Thermo Fisher K-Alpha) with standard Al Kα (1486.7 eV) X-ray source. The binding energies were calibrated using the signal from the adventitious carbon (binding energy C 1 s = 284.6 eV).

XPS spectra were fitted using Gaussian–Lorentzian functions. XPS depth profile was obtained by performing the XPS elemental scan after each 30 s Ar ion of 1000 eV etching. The resolution and sensitivity of XPS instrument is 0.35 eV and 3.7 kcps, which is measured by the full width at half maximum (FWHW). The microstructure and morphology were examined by field emission scanning electron microscopy (FESEM, Ultra 55, ZEISS) in InLens mode with voltage of 3 kV. Energy-dispersive X-ray spectroscopy (EDS) were performed to explore the element distribution in the same SEM system with the voltage of 18 kV. Crystallinity of thin films on Cu foil was analysed by a Rigaku-D/MAX 2000x-ray diffraction (XRD) system with Cu Kα radiation. Transmission electron microscopy (TEM, Tecnai F20 S-Twin, FEI) was conducted to observe the layer-by-layer structure of nanolamintes. The sample for TEM cross-section characterization was prepared by the combination of mechanical grinding and ion beam thinning.

Electrochemical measurements.
2032-type coin half-cells were used for the electrochemical measurements. The pristine ZnO films or ZnO/TiO$_2$ nanolaminates on copper foil were directly used as the working electrodes. A metallic lithium foil served as both the counter electrode and the reference electrode. The porous polypropylene film (Celgard 2500) was used as the separator. A solution of 1 M LiPF$_6$ dissolved in a mixture of ethylene carbonate (EC) and dimethyl carbonate (DEC) (1:1, w/w) was used as liquid electrolyte. The coin cells were assembled in an argon-filled glove box, in which oxygen and water contents were less than 1 ppm. The galvanostatic charge-discharge tests were performed using a battery testing system (LAND CT2001A) at various current densities in the potential range between 0.05 V–2.0 V and 0.05 V–2.5 V. Cyclic voltammetry evaluations (CV) were conducted at the scanning rate of 0.3 mV/s at a voltage between 0 V–3 V using an electrochemical workstation (CHI 660E). Electrochemical impedance spectroscopy (EIS) were taken on the same electrochemical workstation by applying an AC voltage amplitude of 5 mV in the frequency range of 10 mHz ~100 kHz on the open circuit voltage of the cells.

References

1. Poizot, P., Laruelle, S., Grugeon, S., Dupont, L. & Tarascon, J. M. Nano-sized transition-metal oxides as negative-electrode materials for lithium-ion batteries. *Nature* **407**, 496 (2000).
2. Nam, K. T. *et al*. Virus-Enabled Synthesis and Assembly of Nanowires for Lithium Ion Battery Electrodes. *Science* **312**, 885 (2006).
3. Scrosati, B., Hassoun, J. & Sun, Y.-K. Lithium-ion batteries. A look into the future. *Energy & Environmental Science* **4**, 3287–3295 (2011).
4. Li, M., Lu, J., Chen, Z. & Amine, K. 30 Years of Lithium-Ion Batteries. *Advanced Materials* **18**, 3941–3946 (2018).
5. Zhang, W.-M., Wu, X.-L., Hu, J.-S., Guo, Y.-G. & Wan, L.-J. Carbon Coated Fe$_3$O$_4$ Nanospindles as a Superior Anode Material for Lithium-Ion Batteries. *Advanced Functional Materials* **18**, 3941–3946 (2008).
6. Lin, J. *et al*. Graphene Nanoribbon and Nanostructured SnO$_2$ Composite Anodes for Lithium Ion Batteries. *ACS Nano* **7**, 6001–6006 (2013).
7. Zhao, Y. *et al*. Recent Developments and Understanding of Novel Mixed Transition-Metal Oxides as Anodes in Lithium Ion Batteries. *Advanced Energy Materials* **6**, 1502175 (2016).
8. Yue, G. H. *et al*. Flower-like Nickel Oxide Nanocomposites Anode Materials for Excellent Performance Lithium-ion Batteries. *Electrochimica Acta* **152**, 315–322 (2015).
9. Zhang, X. X., Xie, Q. S., Yue, G. H. & Zhang, Y. A novel hierarchical network-like Co$_3$O$_4$ anode material for lithium batteries. *Electrochimica Acta* **111**, 746–754 (2013).
10. Xie, Q. *et al*. Facile fabrication of various zinc-nickel citrate microspheres and their transformation to ZnO-NiO hybrid microspheres with excellent lithium storage properties. *Scientific Reports* **5**, 8351 (2015).
11. Zhang, G. *et al*. High-performance and ultra-stable lithium-ion batteries based on MOF-derived ZnO@ZnO quantum dots/C core-shell nanorod arrays on a carbon cloth anode. *Advanced Materials* **27**, 2400–2405 (2015).
12. Lu, S., Wang, H., Zhou, J., Wu, X. & Qin, W. Atomic layer deposition of ZnO on carbon black as nanostructured anode materials for high-performance lithium-ion batteries. *Nanoscale* **9**, 1184–1192 (2017).
13. Xu, G. L. *et al*. PEDOT-PSS coated ZnO/C hierarchical porous nanorods as ultralong-life anode material for lithium ion batteries. *Nano Energy* **18**, 253–264 (2015).
14. Kushima, A. *et al*. Leapfrog Cracking and Nanoamorphization of ZnO Nanowires during *In Situ* Electrochemical Lithiation. *Nano Letters* **11**, 4535 (2011).
15. Zhang, Y., Wang, Z., Li, Y. & Zhao, K. Lithiation of ZnO nanowires studied by *in-situ* transmission electron microscopy and theoretical analysis. *Mechanics of Materials* **91**, 313–322 (2015).

16. Kundu, S. *et al.* Structural interpretation of chemically synthesized ZnO nanorod and its application in lithium ion battery. *Applied Surface Science* **329**, 206–211 (2015).
17. Kim, J., Hong, S.-A. & Yoo, J. Continuous synthesis of hierarchical porous ZnO microspheres in supercritical methanol and their enhanced electrochemical performance in lithium ion batteries. *Chemical Engineering Journal* **266**, 179–188 (2015).
18. Li, J. *et al.* Metal-organic frameworks derived yolk-shell ZnO/NiO microspheres as high-performance anode materials for lithium-ion batteries. *Chemical Engineering Journal* **335**, 579–589 (2018).
19. Shen, X., Mu, D., Chen, S., Wu, B. & Wu, F. Enhanced electrochemical performance of ZnO-loaded/porous carbon composite as anode materials for lithium ion batteries. *Acs Appl Mater Interfaces* **5**, 3118–3125 (2013).
20. Köse, H., Karaal, Ş., Aydın, A. O. & Akbulut, H. A facile synthesis of zinc oxide/multiwalled carbon nanotube nanocomposite lithium ion battery anodes by sol–gel method. *Journal of Power Sources* **295**, 235–245 (2015).
21. Xie, Q. *et al.* Yolk-shell ZnO-C microspheres with enhanced electrochemical performance as anode material for lithium ion batteries. *Electrochimica Acta* **125**, 659–665 (2014).
22. Xie, Q. *et al.* Electrostatic Assembly of Sandwich-Like Ag-C@ZnO-C@Ag-C Hybrid Hollow Microspheres with Excellent High-Rate Lithium Storage Properties. *Acs Nano* **10**, 1283 (2015).
23. George, S. M. Atomic Layer Deposition: An Overview. *Chemical Reviews* **110**, 111–131 (2010).
24. Johnson, R. W., Hultqvist, A. & Bent, S. F. A brief review of atomic layer deposition: from fundamentals to applications. *Materials today* **17**, 236–246 (2014).
25. Guan, C. & Wang, J. Recent Development of Advanced Electrode Materials by Atomic Layer Deposition for Electrochemical Energy Storage. *Advanced Science* **3**, 1500405 (2016).
26. Meng, X., Yang, X.-Q. & Sun, X. Emerging Applications of Atomic Layer Deposition for Lithium-Ion Battery Studies. *Advanced Materials* **24**, 3589–3615 (2012).
27. Meng, X., Cao, Y., Libera, J. A. & Elam, J. W. Atomic Layer Deposition of Aluminum Sulfide: Growth Mechanism and Electrochemical Evaluation in Lithium-Ion Batteries. *Chemistry of Materials* **29**, 9043–9052 (2017).
28. Li, X. *et al.* Batteries: Tin Oxide with Controlled Morphology and Crystallinity by Atomic Layer Deposition onto Graphene Nanosheets for Enhanced Lithium Storage. *Advanced Functional Materials* **22**, 1646–1646 (2012).
29. Meng, X. *et al.* High-Performance High-Loading Lithium-Sulfur Batteries by Low Temperature Atomic Layer Deposition of Aluminum Oxide on Nanophase S Cathodes. *Advanced Materials Interfaces* **4**, 1700096 (2017).
30. Kong, J.-Z. *et al.* Ultrathin ZnO coating for improved electrochemical performance of $LiNi_{0.5}Co_{0.2}Mn_{0.3}O_2$ cathode material. *Journal of Power Sources* **266**, 433–439 (2014).
31. Cao, Y., Meng, X. & Elam, J. W. Atomic Layer Deposition of Li_xAl_yS Solid-State Electrolytes for Stabilizing Lithium-Metal Anodes. *ChemElectroChem* **3**, 858–863 (2016).
32. Liu, J. *et al.* Atomic Layer Deposition of Lithium Tantalate Solid-State Electrolytes. *The Journal of Physical Chemistry C* **117**, 20260–20267 (2013).
33. Kozen, A. C., Pearse, A. J., Lin, C.-F., Noked, M. & Rubloff, G. W. Atomic Layer Deposition of the Solid Electrolyte LiPON. *Chemistry of Materials* **27**, 5324–5331 (2015).
34. Cao, Y.-Q. *et al.* ZnO/ZnS Core-Shell Nanowires Arrays on Ni Foam Prepared by Atomic Layer Deposition for High Performance Supercapacitors. *Journal of The Electrochemical Society* **164**, A3493–A3498 (2017).
35. Zhao, Y. *et al.* Three dimensional carbon/ZnO nanomembranes foam as lithium-ion anode with long-life and high areal capacity. *Journal of Materials Chemistry A* **6**, 7227–7235 (2018).
36. Yu, M., Wang, A., Wang, Y., Li, C. & Shi, G. An alumina stabilized ZnO-graphene anode for lithium ion batteries via atomic layer deposition. *Nanoscale* **6**, 11419–11424 (2014).
37. Knez, M., Nielsch, K. & Niinistö, L. Synthesis and surface engineering of complex nanostructures by atomic layer deposition. *Advanced Materials* **19**, 3425–3438 (2007).
38. Elam, J., Sechrist, Z. & George, S. ZnO/Al$_2$O$_3$ nanolaminates fabricated by atomic layer deposition: growth and surface roughness measurements. *Thin Solid Films* **414**, 43–55 (2002).
39. Chen, Z., Belharouak, I., Sun, Y. K. & Amine, K. Titanium-Based Anode Materials for Safe Lithium-Ion Batteries. *Advanced Functional Materials* **23**, 959–969 (2013).
40. Zhang, Y., Tang, Y., Li, W. & Chen, X. Nanostructured TiO2-based Anode Materials for High-performance Rechargeable Lithium-ion Batteries. *Chemnanomat* **2**, 764–775 (2016).
41. Cao, Y. Q. *et al.* Photocatalytic activity and photocorrosion of atomic layer deposited ZnO ultrathin films for the degradation of methylene blue. *Nanotechnology* **26**, 024002 (2015).
42. Qin, C. C. *et al.* Improvement of electrochemical performance of nickel rich $LiNi_{0.6}Co_{0.2}Mn_{0.2}O_2$ cathode active material by ultrathin TiO_2 coating. *Dalton Transactions* **45**, 9669–9675 (2016).
43. Nefedov, V. I., Salyn, Y. V., Leonhardt, G. & Scheibe, R. A comparison of different spectrometers and charge corrections used in X-ray photoelectron spectroscopy. *Journal of Electron Spectroscopy & Related Phenomena* **10**, 121–124 (1977).
44. Guo, X. *et al.* Porous TiB$_2$-TiC/TiO$_2$ heterostructures: Synthesis and enhanced photocatalytic properties from nanosheets to sweetened rolls. *Applied Catalysis B: Environmental* **217**, 12–20 (2017).
45. Strohmeier, B. R. & Hercules, D. M. Surface spectroscopic characterization of the interaction between zinc ions and γ-alumina. *Journal of Catalysis* **86**, 266–279 (1984).
46. Wagner, C. D., Zatko, D. A. & Raymond, R. H. Use of the oxygen KLL Auger lines in identification of surface chemical states by electron spectroscopy for chemical analysis. *Analytical Chemistry* **52**, 1445–1451 (1980).
47. Yan, X. *et al.* The interplay of sulfur doping and surface hydroxyl in band gap engineering: Mesoporous sulfur-doped TiO$_2$ coupled with magnetite as a recyclable, efficient, visible light active photocatalyst for water purification. *Applied Catalysis B: Environmental* **218**, 20–31 (2017).
48. Fu, Z. W., Huang, F., Zhang, Y., Chu, Y. & Qin, Q. Z. The Electrochemical Reaction of Zinc Oxide Thin Films with Lithium. *Journal of the Electrochemical Society* **150**, A714–A720 (2003).
49. Li, N., Jin, S. X., Liao, Q. Y. & Wang, C. X. ZnO anchored on vertically aligned graphene: binder-free anode materials for lithium-ion batteries. *ACS Applied Materials & Interfaces* **6**, 20590–20596 (2014).
50. Wu, M.-S. & Chang, H.-W. Self-Assembly of NiO-Coated ZnO Nanorod Electrodes with Core–Shell Nanostructures as Anode Materials for Rechargeable Lithium-Ion Batteries. *The Journal of Physical Chemistry C* **117**, 2590–2599 (2013).
51. Wang, Y., Jiang, X., Yang, L., Jia, N. & Ding, Y. *In situ* synthesis of C/Cu/ZnO porous hybrids as anode materials for lithium ion batteries. *ACS Applied Materials & Interfaces* **6**, 1525–1532 (2014).
52. Qiao, L. *et al.* Single electrospun porous NiO-ZnO hybrid nanofibers as anode materials for advanced lithium-ion batteries. *Nanoscale* **5**, 3037–3042 (2013).
53. Liu, Z. *et al.* Dramatically Enhanced Li-Ion Storage of ZnO@C Anodes through TiO$_2$ Homogeneous Hybridization. *Chemistry-A European Journal* **25**, 582–589 (2019).
54. Huang, G., Xu, S., Lu, S., Li, L. & Sun, H. Porous polyhedral and fusiform Co$_3$O$_4$ anode materials for high-performance lithium-ion batteries. *Electrochimica Acta* **135**, 420–427 (2014).
55. Tan, H., Cho, H. W. & Wu, J. J. Binder-free ZnO@ZnSnO$_3$ quantum dots core-shell nanorod array anodes for lithium-ion batteries. *Journal of Power Sources* **388**, 11–18 (2018).

56. Wang, B. *et al.* An efficient route to a hierarchical $CoFe_2O_4$@graphene hybrid films with superior cycling stability and rate capability for lithium storage. *Electrochimica Acta* **146**, 679–687 (2014).
57. Hsieh, C. T., Mo, C. Y., Chen, Y. F. & Chung, Y. J. Chemical-wet Synthesis and Electrochemistry of $LiNi_{1/3}Co_{1/3}Mn_{1/3}O_2$ Cathode Materials for Li-ion Batteries. *Electrochimica Acta* **106**, 525–533 (2013).
58. Wu, X., Li, S., Wang, B., Liu, J. & Yu, M. One-step synthesis of the nickel foam supported network-like ZnO nanoarchitectures assembled with ultrathin mesoporous nanosheets with improved lithium storage performance. *RSC Advances* **5**, 81341–81347 (2015).

Acknowledgements

Author Contributions

Y.Q.C. and S.S.W. carried out the sample fabrication and electrochemical measurements. C.L. conducted XPS test. A.D.L. and D.W. participated in the discussion of results. Y.Q.C. drafted the manuscript. A.D.L. supervised the whole work and revised the manuscript. All authors critically read and commented on the manuscript.

Additional Information

Supplementary information accompanies this paper at https://doi.org/10.1038/s41598-019-48088-2.

Competing Interests: The authors declare no competing interests.

Publisher's note: Springer Nature remains neutral with regard to jurisdictional claims in published maps and institutional affiliations.